Pulse rejection for millimeter wave Doppler radars

V. Venkatesh*, S. Tanelli*, H. Hovhannisiyan * †, G. Masalias Huguet * ‡

* Jet Propulsion Laboratory, California Institute of Technology, Pasadena, CA.

† University of California at San Diego, CA.

‡ University of Massachusetts, MA.

Abstract—

While short wavelengths allow for compact radar sensors, they also reduce unambiguous Doppler velocity. This work investigates a W-band radar that transmits two closely spaced pulses within a repetition time and retrieves Doppler velocity by cross-correlating received voltages corresponding to the same range-bin. Significantly larger unambiguous Doppler velocities can now be obtained provided mechanisms to reject inter-pulse interference are developed. Following up from the unsatisfactory performance of an up/down chirp pulse compression orthogonal waveform pair, two pulse rejection techniques are investigated herein and potential applications explored. The first technique transmits pulses at offset frequencies, while a digital filter isolates receive echoes from each pulse. Based on theoretical error analysis and simulations, the frequency diverse Doppler velocity estimation technique is shown to be limited to scatterers that have a response limited in range such as surfaces with low RMS heights such as the Mars landing site when observed with a beam-limited geometry. This is consistent with the reported use of this technique with dominant metallic scatterers encountered by automotive radars wherein range-limited scatterers give rise to small phase fluctuations, thereby muting fading of the received signal. The second technique uses the starting phase of a sinusoidal waveform to encode two orthogonal channels over N pulses within the dwell. Closed-form expressions for inter-channel isolation are derived and compared with Monte-Carlo simulations. Based on simulations and theoretical analysis, the starting phase velocimetry technique is shown to be a viable candidate for space-borne cloud Doppler radars. The use of a lag that is exactly half the pulse repetition time allows for a cross-spectral algorithm which is superior to time-domain cross-correlation algorithms at millimeter wavelengths. A significant advantage of the starting phase pulse rejection Doppler velocity measurement technique is that it requires no additional RF hardware relative to what is already available in typical space-borne radar systems. We note that the simulated 20 dB isolation of this technique corresponding to 1.5 km along-tack resolution warrants further research. Notwithstanding, the starting phase based pulse rejection technique can be viewed as a superimposable method in NASA's toolkit to potentially enable the first space-borne Doppler velocity measurements in clouds.

Index Terms—**Millimeter wave radar, signal processing, Monte-Carlo simulation.**

I. INTRODUCTION

From Viking to the Mars Science Laboratory, trends in planetary missions point toward simpler landing gear and increasingly sophisticated sensors [1]. For example, the first Viking lander used air bags to deliver the payload to the Martian surface [2] while the Mars Science Lab (MSL) used an air-crane maneuver to the same end [3]. Low cost asteroid

Corresponding author email : vijay.venkatesh@jpl.nasa.gov .

mining missions [4] may further restrict instrument mass and size in the future. One path to miniaturizing the radar sensor is to increase the frequency beyond the Ka-band design used on MSL. This enables physically smaller antennas for the same angular resolution. But shorter wavelengths λ also reduce the unambiguous Doppler velocity v_u. This is because v_u equals $\frac{\lambda}{4T}$ for radars that transmit a train of pulses at a fixed pulse repetition time T. However, T cannot be reduced indiscriminately because of its direct proportionality to unambiguous range R_u for the pulse-pair method ($R_u = \frac{cT}{2}$, where c is the velocity of light in free space) . For this reason, there is significant interest in techniques that increase the unambiguous Doppler velocity v_u by decoupling it from range coverage R_u.

The need to decouple v_u from R_u is also central for space-borne Doppler velocity estimation in clouds, which are yet to be demonstrated [5] [6][7] [8]. The difficulty herein is the combination of rapid platform motion and finite antenna size [9]. These attributes cause space-borne cloud and precipitation radars to encounter significantly wider Doppler spectra relative [10][11] to their air-borne [12] and ground based counterparts [13]. To illustrate the notion of spectral broadening due to space-craft motion, consider the Doppler spectrum measured by a nadir looking antenna of infinite size flying on a rapidly moving space-craft. In this hypothetical scenario, the space-craft motion is perfectly orthogonal to the "pencil" radar beam and the measured Doppler spectrum is solely meteorological. For the more realistic scenario of a finite sized antenna flying on a rapidly moving platform, the projection of massive spacecraft velocity along the continuum of angles within the antenna mainlobe superimposes and overwhelms the meteorological Doppler spectrum. By the Wiener-Khinchine theorem, the Doppler spectrum and the correlation function form a Fourier pair [14]. This broad Doppler spectrum due to space-craft motion consequently leads to such narrow correlation functions that there is little coherence on time-scales needed to sample the entire troposphere [15].

The Polarization Diverse Pulse-Pair (PDPP) algorithm transmits a two-pulse train with orthogonal polarizations during each transmit and receive cycle [16] [17]. The idea is that two pulses separated by a small time lag (τ) provide adequate sampling of the Doppler spectrum, while the pulse repetition time (T) can be adjusted independently for range coverage to adequately sample the troposphere. The PDPP algorithm also needs additional RF hardware such as an orthomode transducer, a high power switch to interleave polarizations, dual-polarization capability for the antenna and a second millimeter wave receive chain. The net result of all this is increased mass

and complexity in achieving cross-polarization isolation at millimeter wavelengths. Orthogonal waveforms have been investigated as a mechanism to mitigate inter-channel interference for high resolution imaging using synthetic aperture radars (SAR) [18] [19] and multiple-input-multiple-output (MIMO) radars [20][21][22] . But these applications had the luxury of long chirp lengths and employed pulse compression to synthesize orthogonal waveforms. In pulsed radar applications that probe targets as close as 100 meters, the use of pulse compression to synthesize orthogonal channels is often impractical.

In this work, short sinusoidal bursts are employed to synthesize orthogonal waveforms. Approaches to pulse rejection velocimetry using frequency and starting phase diversity are investigated. The frequency diversity velocimetry algorithm was first developed for point-like targets [23] and has recently been empirically demonstrated on surfaces [24]. While [25] applies frequency diversity velocimetry to simulated cloud echoes using a large 35 meter antenna, its practical feasibility for clouds remains unclear. The mathematical framework developed in this work allows quantitative assessment of frequency diversity velocimetry performance for various applications as a function of instrumental parameters. Similarly, the starting phase diverity scheme used herein was first introduced in [26], and there has since been a gradual progression in its capability [27][28][29][30]. The use of specific starting phase codes for range ambiguity mitigation has been demonstrated [30][27] in ground based weather radars. Similar techniques have been engineered into phase coherent transmitters to improve polarimetric measurements of weather [31] [32] [33]. The novel part herein is the application of the starting phase diversity technique to to space-borne Doppler velocity measurements in cloud and precipitation echoes. The following section presents an over-arching notional framework for pulse rejection velocimetry. The performance of frequency diversity velocimetry and starting phase velocimetry are investigated using theoretical analysis and numerical simulations [34][24].
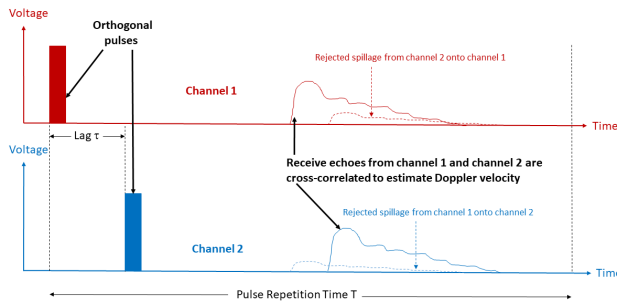
II. ORTHOGONAL WAVEFORM VELOCIMETRY

Fig. 1: Illustration of the pulse rejection concept to estimate Doppler velocity. First, the pulse filtering operation isolates the corresponding Tx/Rx channels by rejecting inter-channel interference. Next, the phase changes between echoes corresponding to the same range provide a measure of velocity over an unambiguous Nyquist interval of $\frac{\lambda}{4\tau}$, while the unambiguous range is still $\frac{cT}{2}$.

Fig. 1 depicts the approach to Doppler velocity retrieval using pulse rejection as a means to estimate phase change across short time-lags. The idea is that cross-correlation of the received voltages corresponding to the same range yields estimates of Doppler velocity. The two channels are encoded to reject inter-channel interference but pass the "right" signal. Each channel uses a filter x based on the transmitted signal such that

$$v_i(t) = w_i(t) \oplus x_i(t) \quad \forall \quad i = 1, 2 \tag{1}$$

where w and v are the received voltages before and after the filtering operation. The filtering operator $\oplus$ is either a convolution or a dot product depending on the implementation of orthogonality. This orthogonality constraint minimizes spillage from one channel to the other and is denoted by

$$|\langle w_i(f) \cdot x_j(f) \rangle| \approx 0 \quad \forall \quad i \neq j. \tag{2}$$

Here, $w_i(f) = \int_\infty^\infty w_i(t) \, e^{-2j\pi f t} dt$ is the Fourier transform of the time-domain signal $w_i(t)$. A similar definition follows for $x_j(t)$. After the filtering operation, cross-correlation of the signals from the two channels allows estimation of Doppler velocity. To achieve Doppler velocity precision comparable to traditional pulse pair Doppler measurements, we must retain coherence such that $v_1(t) \cdot v_2(t + \tau) \approx v_1(t) \cdot v_1(t + \tau)$. The filter design constraints imposed by equations (1-2) can be solved with two different approaches. First, pulse compression techniques provide an SNR improvement while also satisfying the afore mentioned constraints. Second, frequency and starting phase diversity satisfy the constraints by rejecting inter-channel spillage alone and do not improve SNR.

Fig. 2 shows simulated results from pulse compression orthogonal waveform channel synthesis using matched filtering operators in equation (2). Up and down chirps were used to approximate orthogonal waveforms in this simulation. While the point target response in Fig. 2 shows reasonable inter-channel isolation of 20 dB, the pulse-limited surface response of the pulse compression orthogonal waveform pair shows significantly degraded inter-channel isolation of approximately 5 dB. The is because inter-channel spillage power adds up in range as the range extent of scatterers increases. The failure of the up/down chirp pair and the less than desirable isolation reported in the application of many pulse compression based orthogonal waveforms to space-borne radars [18] are important stepping stones in engineering the next generation of space-borne radars. While it is conceivable that future research opens the doors to pulse compression based orthogonal waveform pairs that are robust to scatterer ubiquity, there is also a need for orthogonal waveform synthesis without the use of pulse compression. Fig. 3 shows results from pulse rejection based orthogonal waveform pair synthesis. Simulated results of two pulse rejection implementations that use frequency and starting phase diversity to synthesize orthogonal channels are overlaid. Three comments are in order. First, it is clear that both pulse rejection techniques investigated in this work succeed where prior failures of pulse compression based orthogonal channel synthesis have been reported [18]. Second, the technique employed in synthesizing channels 1 and 2 uses random starting
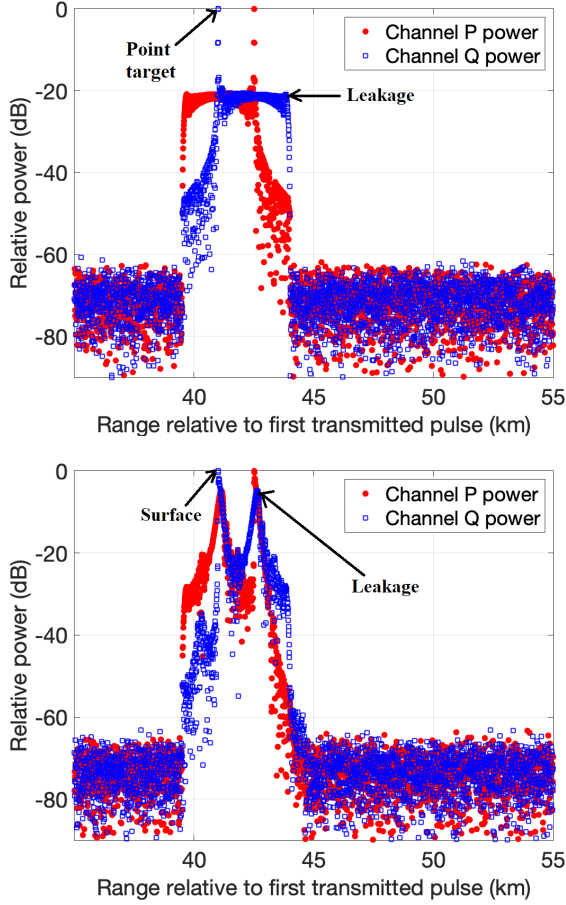
Fig. 2: Simulation of pulse compression orthogonal waveform response from a point target and pulse-limited surface. Up and down chirps of bandwidth 10 MHz were employed. As the range extent of the response increases from a point-target to a pulse-limited surface, inter-channel leakage increases.
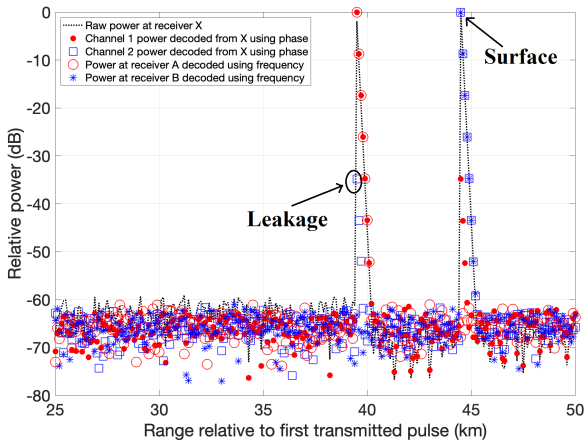

Fig. 3: Simulation of pulse rejection orthogonal waveform response from a pulse-limited surface. Both the frequency and starting phase diversity pulse rejection techniques show much better inter-channel isolation than the pulse compression orthogonal waveforms in Figure 2.

phase to synthesize orthogonal channels over the duration of the dwell. A matched filter operator is correspondingly used in equation (1). As implied in Fig. 3, an advantage of this method is that it only needs a single receiver. With the starting phase diversity technique, inter-channel isolation comparable to 30 dB is obtained with relatively short dwell times of 100 ms for low spectrum width. Third, the frequency diversity technique employs a convolution operator in equation (1) to filter echoes based on orthogonality and requires pulses that are separable in the frequency domain [24]. Although Fig. 3 shows that the frequency diversity technique obtains inter-channel isolation greater than 50 dB, this comes at the expense of coherence. Given the lack of analytical literature on the exact functional form of the coherence loss, the following section analytically explores potential applications for the frequency diversity technique.

III. FREQUENCY DIVERSITY VELOCIMETRY

Frequency diversity velocimetry uses 2 offset frequencies to synthesize orthogonal channels [24] [25]. First introduced in [23] for point-like scatterers, it has subsequently been considered for distributed targets in[24][25]. Assume two pulses with center frequencies f_1 and f_2 separated by a short lag τ in the first pulse repetition time (PRT). While retaining the same lag τ, the order of pulses is then reversed every pulse repetition time T. Covariance estimates from the f_1/f_2 sequence $c_{12}(\tau)$ and the f_2/f_1 sequence $c_{21}(\tau)$are used to estimate Doppler phase and velocity. This approach relies on the assumption that the ensemble of scatterers within the resolution volume remains sufficiently coherent over T so that the two covariances are highly anti-correlated. As discussed in [24], its application to distributed targets is constrained by this fundamental assumption, and the experimental data shown therein provided examples of coherence loss in two sources of scattering : rough surface scattering as observed from an air-borne platform and volumetric Rayleigh/Mie scattering from cloud particles. This affects studies such as [25] which studies its application to a notional geostationary weather radar without accounting for the fact that approximations developed for point-like targets in [24] do not extend to volumetric scattering. Point-targets allow high coherence to be maintained over T, and allows the accuracy of the Doppler velocity estimates be experessed as a function of τ and SNR while being relatively independent of T.

A key question that remains unanswered is - under which conditions can frequency diversity velocimetry provide advantages relative to single-frequency applications ? To analytically evaluate errors in pulse rejection velocimetry, we use already existing expressions in the literature that relate the correlation function to the Doppler velocity estimate standard deviation [41][see equation (36 in section IV)]. Since there is no volumetric scattering based correlation model in the literature that accounts quantitatively for the loss in coherence due to frequency diversity, we derive it herein. Consider a notional nadir looking radar system pointed directly at an electrically rough surface. The illuminated surface is assumed to be beam-limited such that we can neglect the dependence

of normalized radar cross section σ_0 on incidence angle. In the geometry in Fig. 4, we define origin to be the center of the resolution volume. Let the antenna phase center be located at $(0, 0, -z_T)$. Assuming wide-sense stationarity, the cross-correlation of signals C_{12}^S corresponding to wavenumber k_1 and k_2 can we written as

$$c_{12}^S(\tau) = \frac{\langle V_1(t)V_2^*(t+\tau)\rangle}{\sqrt{\langle V_1^2\rangle\langle V_2^2\rangle}} \quad (3)$$

Following [42], the received voltage V_1 in equation (3) at the antenna due to backscattering from the surface given by

$$V_1(t) = K\sigma_0 \int_{V''} A_1(r'')W(r'')\exp\{-2jk_1|\vec{R} + \vec{r''}(t)|\}dV'', \quad (4)$$

where K denotes an instrument dependent constant, k_1 denotes the radar wavenumber and $|\vec{r''}|$ denotes the distance from the radar antenna phase-center to the scatterer. We note that we have neglected the dependence of the normalized radar cross-sections σ_0 on incidence angle. This appears reasonable since the beamwidths probing the resolution volume are narrow. Further, surfaces appear electrically very rough at W-band and the scattering cross-section of individual facets have a weak dependence on incidence angle. As the scatterers advect, these distances change as a function of time and subsequently produce fading of the voltage V_1. The antenna and range weighting functions in (4) are given by

$$A(r'') = g\exp\{-\frac{x''^2(t)}{4r_0^2\sigma_{e\phi}^2} - \frac{y''^2(t)}{4r_0^2\sigma_\theta^2}\} \quad (5)$$

where g is the effective gain of the two-way antenna pattern. Here, x'' and y'' the horizontal co-ordinates that specify the location of the surface scatterer facet. The symbols σ_ϕ and σ_θ are the second central moments of the two-way antenna patterns in the azimuth and elevation planes respectively plane. In turn, these are related to two-way antenna beamwidth by the relationship $\sigma_{e\phi} = \frac{\phi_{3dB}}{\sqrt{16ln2}}$. Here, ϕ_{3dB} is the one-way 3-dB antenna beamwidth in the azimuthal plane. To proceed, we allow the scattering to be volumetric with a range extent σ_R. As the range resolution becomes infinitesimal, the volumetric scattering collapses into a surface response. The effective range weighting function can therefore be written as [49]

$$W(r'') = \exp\{-\frac{z''^2(t)}{4\sigma_R^2}\}. \quad (6)$$

Since the spatial integral dV in equation (4) is seperable in the x'', y'' and z'' co-ordinates, V_1 can be simplified as

$$V_1(t) = K\sigma_0 \exp\{-2jk_1r_0\} I_{x_1}(t)I_{y_1}(t)I_{z_1}(t) \quad (7)$$

where, I_{x_1}, I_{y_1}, I_{z_1}, I_{x_2}, I_{y_2} and I_{z_2} are defined in the appendix. Similarly, the backscattered voltage $V_2(t+\tau)$ is written as

$$V_2(t+\tau) = K\sigma_0 \left(\int_{V''} A_2(r'')W(r'') \right.$$
$$\left. \exp\{-2jk_2(|\vec{R} + r''(\vec{t + \tau})|\}dV'', \right) \quad (8)$$

$$V_2(t+\tau) = K\ \sigma_0\ (\ \exp\{-2jk_2r_0\}$$
$$I_{x_2}(t+\tau)I_{y_2}(t+\tau)I_{z_2}(t+\tau)) \quad (9)$$

To evaluate the expectation $\langle V_1V_2^*(\tau)$ in equation (**??**), we must account for weighting of scatterers within the resolution volume corresponding to V_1 at time t and V_2 at time $t + \tau$. Note that time t and range R are inter-changable provided a scaling constant is employed. Consistent with the definition in equation (3), we postpone the evaluation of temporal expectation and begin by expressing the spatial co-integration [35] as

$$\int_{v'} V_1(\vec{R})V_2^*(\vec{R} + \vec{v}\tau)dv' = J_x \cdot J_y \cdot J_z, \quad (10)$$

where dv' is an elemental volume within the resolution cell V'. Here, $\vec{v}$ captures the relative motion of scatterers with respect to the radar platform. The integral in equation (10) is simplified using a Taylor series expansion about origin indicated in Fig. 4 to approximate the phase term and evaluated in the appendix. The resultant integrals are evaluated using well known identities for integrals in [36]. The expected value of the covariance $V_1V_2^*(\tau)$ is then computed as

$$\langle J_x \cdot J_y \cdot J_z\rangle = J_x \cdot J_y \cdot \int_{-\infty}^{\infty} J_z p_{v_{tz}}dv_{tz}. \quad (11)$$

Equation (11) neglects temporal fluctuations in x and y and only evaluates the expectation over z. This is reasonable given that changes in z result in much higher phase changes relative to x and y. Further, the V_1 and V_2 terms in the denominator of (3) are calculated using the same antenna and range weighting function definitions used to calculate J_x, J_y and J_z.

Symbol	Meaning	units
k_1	Radar wavenumber corresponding to frequency 1	m^{-1}
k_2	Radar wavenumber corresponding to frequency 2	m^{-1}
δk	Difference between k_2 and k_1 radar wavenumbers	m^{-1}
K	Radar constant	Vm^{-2}
σ_0	Normalized radar cross section of surface	m^2
g	Effective two-way antenna gain	
r_0	Range to resolution volume	m
x''	x-coordinate of scatterer location	m
y''	y-coordinate of scatterer location	m
z''	z-coordinate of scatterer location	m
r''	Scatterer location as a function of x'', y and z''	m
$\sigma_{e\phi}$	Second central moment of two-way azimuth pattern	rad
$\sigma_{e\theta}$	Second central moment of two-way elevation pattern	rad
σ_R	Range extent of scattering within resolution cell	m
v_x	Velocity component along x''	ms^{-1}
v_y	Velocity component along y''	ms^{-1}
v_z	Velocity component along z''	ms^{-1}
σ_{t_z}	RMS turbulent velocity along z''	ms^{-1}

Fig. 4: Illustration of the coordinate system used in the theoretical formulation herein. Origin (indicated by the blue rectangle) is located at the center of the resolution volume. For convenience, the radar is assumed to be pointed orthogonal to the surface. Symbols used in modeling the correlation between two complex voltages at frequencies f_1 and f_2 are indicated in the table.

Following the evaluation of spatial integrals in equation (7), (9) and (11) in the appendix, the covariance magnitude and phase of the f_1/f_2 sequence is finally given by

$$|\langle c_{12}^S(\tau)\rangle| = P\ exp\Big[-\frac{2v_x^2\tau^2 k_2^2\sigma_{e\phi}^2}{2\delta k^2 r_0^2\sigma_{e\phi}^2 + 1}\Big]exp\Big[-\frac{2v_y^2\tau^2 k_2^2\sigma_{e\theta}^2}{2\delta k^2 r_0^2\sigma_{e\theta}^2 + 1}\Big]$$
$$\cdot\ exp\Big[-2k_2^2\sigma_{tz}^2\tau^2\Big]\cdot exp\Big[-2\sigma_R^2\delta k^2\Big] \tag{12}$$

and

$$\angle\langle c_{12}^S(\tau)\rangle = -2\ \delta k r_0 - k_2\ \delta k\ v_x^2\ \tau^2 - k_2\ \delta k\ v_y^2\ \tau^2 - 2k_2 v_{mz}\ \tau. \tag{13}$$

where P is the backscattered signal power and equations (12)-(13) are derived in the appendix. Here, I_{x1}, I_{y1} and I_{z1} represent the x, y and z components of the volume scattering integral of voltage V_1. Similarly, I_{x2}, I_{y2} and I_{z2} represent the x, y and z components of the volume scattering integral of voltage V_2.). Recall that the order of transmission is reversed every pulse repetition time. The covariance magnitude and phase of the f_2/f_1 sequence are given by

$$|\langle c_{21}^S(\tau)\rangle| = V_1(T)\ V_2^*(T + \tau)$$
$$= C\ \sigma_0\ (\ exp\{-2j\ [k_1 - k_2]r_0\} \tag{14}$$
$$\cdot\ J_x J_y J_z)$$

with phase

$$\angle\langle c_{21}^S(\tau)\rangle = 2\ \delta k r_0 - k_1\ \delta k\ v_x^2\ \tau^2 - k_1\ \delta k\ v_y^2\ \tau^2 - 2k_1 v_{mz}\ \tau. \tag{15}$$

To estimate Doppler velocity, we assume the random process to be wide-sense stationary and omit the dependence on starting time T. Now, consider the estimator

$$\langle c^S(\tau)\rangle = \frac{1}{M}\sum_{i=1}^{M}\Big[c_{12}(\tau) + c_{21}(\tau)\Big] \tag{16}$$

where the number of pulses M is sufficiently large such that the ensemble average approximates the expected value. Denote the phase of $c(\tau)$ as $\Delta\Phi$, the phases of $c_{12}(\tau)$ and $c_{21}(\tau)$ as $\Delta\phi_{12}$ and $\Delta\phi_{21}$, respectively. Assuming that $|\langle c_{12}(\tau)\rangle| = |\langle c_{21}(\tau)\rangle|$, the expected value of phase in equation (8) can be expressed as

$$\angle\langle c_{12}^S(\tau)\rangle + \angle\langle c_{21}^S(\tau)\rangle = \langle\Phi\rangle$$
$$= \big(-[2\{k_1 + k_2\}\ v_{mz}\ \tau$$
$$+ \{k_1 + k_2\}\ \delta k\ v_x^2\ \tau^2$$
$$+ \{k_1 + k_2\}\ \delta k\ v_y^2\ \tau^2\ ]\big). \tag{17}$$

Application of equation (17) becomes practical under the assumption that $\tau\delta k(v_x^2 + v_y^2) \ll v_e$ (non-dimensional), where v_e is the required error on vertical velocity estimation. The implementation we consider herein typically has frequencies that are separated by several MHz for a millimeter wave radar, such as a 94 GHz W-band radar system. The relative bias in the Doppler velocity estimate due to neglecting the second and third terms in equation (9) increases as the vertical velocity approaches 0 m/s, but is negligible for well chosen τ and δk. Neglecting the second and third terms, equation (9) now simplifies to
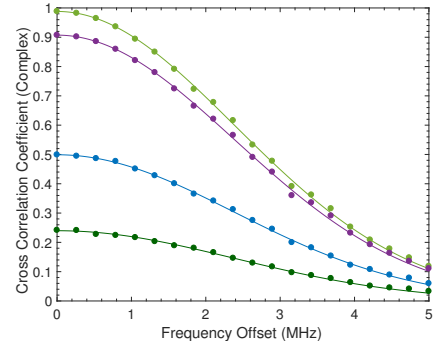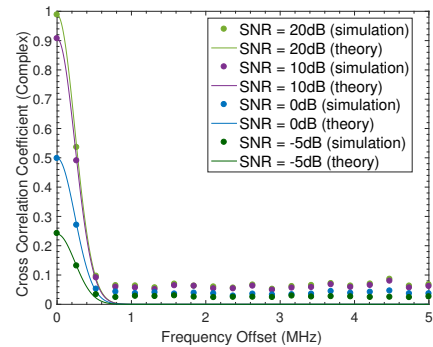
$$\langle\Phi\rangle \simeq -4k_2 v_{mz}\tau. \tag{18}$$
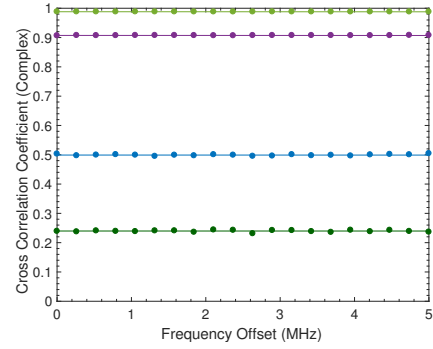
(a) $\sigma_R = 0.1$m
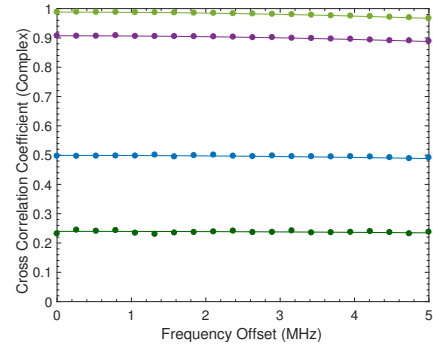
(b) $\sigma_R = 1$m

(c) $\sigma_R = 10$m

(d) $\sigma_R = 100$m

Fig. 5: Comparison of the theoretical cross-correlation model with Monte-Carlo simulations. Results are shown for a lag of 20 micro-seconds, antenna 3-dB beamwidth of 2 degrees and $v_{tz} = 1$ m/s. For this illustration, v_x, v_y and v_z were set to 5 m/s while range r_0 was set to 10 km. Both theory and simulations indicate high coherence for scatterers that are range-limited (i.e. $\sigma_R \leq 1$ m.). However, coherence is lost for scatterers with $\sigma_R = 100$ m.
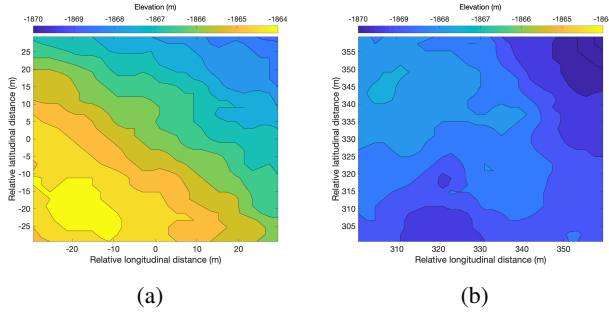
(a)　　　　　(b)

Fig. 6: Digital Elevation Model (DEM) neart the Mars Science Laboratory landing site showing height variations over staial scales comparable to a 1 degree antenna footprint from a 1 km altitude (a) DEM centered at the landing site corresponds to an RMS height of $1.22\ m$ (b) DEM away from the landing site and along the flight track corresponding to RMS height of $0.6\ m$.

(a) Spectrum Width = 1 m/s
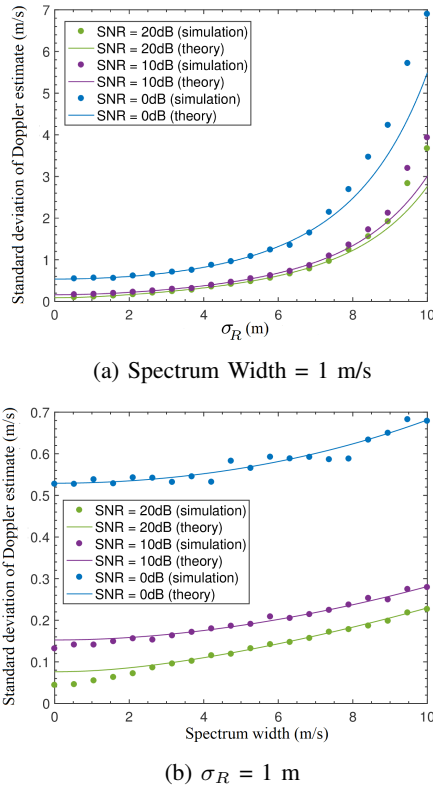

(b) σ_R = 1 m

Fig. 7: Performance of the frequency diverse pulse-pair Doppler estimation algorithm as a function of (a) Range extent of scatterers and (b) Spectrum Width. Simulation parameters employed : δf = 5 MHz, τ = 16 us, dwell time = 100 milliseconds. SNR is as indicated.

$$v_{mz} = -\frac{1}{4k_2\tau}\langle\Phi\rangle. \qquad (19)$$

This final expression in equation (19) is consistent with the point-target based model used in [24] and [25]. But unlike earlier work, we are able to access the precision of the Doppler velocity estimator in equation (19) by using the forward correlation model derived in equations (59), (61) and (62) of the appendix.

Fig. 5 compares the theoretical correlation model developed to Monte-Carlo simulations [34] of the cross-correlation between the received voltages at the two frequencies. For a frequency diversity of 5 MHz, we see that coherence is only preserved if the range extent of scattering $\sigma_R \leq 1$ m. However, the bandwidth of the transmit pulse must be significantly less than 5 MHz for the pulses to be meaningfully separable in the frequency domain. This in turn makes the achievable range resolution based on waveform design to be too coarse relative to the requirements for frequency diverse velocimetry. But scatterers with range spreads that are limited to less than a meter provide an alternate mechanism to meet the requirements for frequency diversity velocimetry. For example, surfaces with low root mean square (RMS) heights have impulse responses that are naturally limited in range extent provided the antenna beamwidth is sufficiently small to adopt a beam limited approximation to the footprint definition [37]. Under these conditions, smooth solid planetary landing sites are suitable for probing with frequency diverse velocimetry at near-nadir geometries. For off-nadir velocimetry, the stated requirement of a small σ_R would result in even more stringent requirements on antenna beamwidth. Fig. 5a-b show that there is little loss in coherence for cases with little range spreads. This is qualitatively consistent with empirical demonstrations of frequency diverse velocimetry on surfaces [24] and point-like scatterers [23]. But as the range spread gets larger, the loss in coherence becomes a stronger function of frequency diversity. For example, nearly all coherence is lost at frequency offsets larger than 1 MHz for scatterer range spread of 100 meters. Fig. 5d is also consistent with literature reporting the use of frequency diversity for procuring more independent samples in cloud and precipitation radars with range resolution comparable to 100 m [38] [39] [40].

To evaluate the performance of the frequency diverse velocimetry algorithm in Fig. 6, we use existing theory in [41] which expresses the precision of the Doppler estimate in terms of the correlation coefficient. The forward model correlation for signals at two frequencies f_1 and f_2 at lag τ is used in lieu of the traditional single-tone correlation model [42]. Both theory and Monte-Carlo simulations indicate that the algorithm performs well for resolution volumes with range spread of the order of a meter. As the range spread becomes larger, the error in the Doppler velocity estimate increases nearly exponentially due to loss of coherence. Fig. 7a shows that Doppler estimates have poor fidelity when the range extent of scattering exceeds 5 m. Given that the skin depth for solid terrain is much smaller than a meter at W-band, the range spread of the backscattered signal can be limited to a few m at nadir provided antenna beamwidths of the order of a degree are employed [37]. For example, Fig. 6 shows inherent height variations for planetary terrain such as the Gale crater on Mars over typical observation scales corresponding to a nominal beam-footprint at 1 km. Fig. 6a and 6b show examples where the RMS heights correspond to $1.22\ m$ and $0.6\ m$ respectively, albeit there is topographic and observation scale variation as the radar footprint traverses a ground track during descent. But

even in these cases, the error in Doppler velocity estimation from frequency diverse velocimetry is a function of spectrum width. As the spectrum width increases due to the combination of high platform speeds and coarse beamwidth, Fig. 6b shows that the precision deteriorates gracefully provided the source of scattering is range limited.

The theoretical results obtained here are consistent with the application of frequency diverse velocimetry to point-like scatterers in the automotive radar community [23] and observational evidence demonstrating feasibility for nearly static surfaces [24]. The empirical nature of earlier investigation in [24] provided a limited understanding of the differences in performance due to scattering from surfaces and clouds. Although the frequency diversity velocimetry algorithm was not developed for cloud radar applications, [25] takes the algorithm originally developed in [24] and applies it to a Ka-band space-borne cloud profiling radar. Based on the results derived in this work, it is now clear that the frequency diverse algorithm investigated herein is more suited for range limited scatterers such as solid surfaces with low RMS roughness and point-like scatterers. However, volume scattering from hydrometeors does not meet the range-limited criterion for scattering naturally. While frequency hopping schemes for independent sample procurement have largely been empirical to date [43], the analytical model relating frequency and coherence can provide value to engineer a spread-spectrum radar. For example, the coherence model shows that a frequency hopping scheme will require more bandwidth for millimeter wavelength landing radar surface observations relative to cloud radar observations [44].

IV. PHASE DIVERSITY VELOCIMETRY

Phase diversity velocimetry uses the starting phase of sinusoidal transmitted waveforms to synthesize two channels that are orthogonal over N pulses in the dwell [28][29][30]. A key property is that channels synthesized by phase diversity velocimetry are not instantaneously orthogonal within each pulse repetition time. Two sinusoidal waveforms with unique starting phases are transmitted separated by a short lag τ. The history of these starting phases for each channel is known ahead of time and removed on receive using a matched filter. Covariance estimates from the matched filtered channels are subsequently used to estimate Doppler velocity. While the variance of the Doppler velocity estimator has been analytically treated in the existing literature, inter-channel isolation is an equally important metric to assess the performance of phase diverse velocimetry.

We compute a closed form expression for inter-channel isolation, since the existing literature does not treat it analytically. Assume impulse transmit voltages T_1 and T_2 at the two channels for pulse number n as

$$T_1(n) = e^{j\phi_1(n)}, \tag{20}$$

$$T_2(n) = e^{j\phi_2(n)}. \tag{21}$$

Here, the starting phase of the channels $\phi_1(n)$ and $\phi_2(n)$ are randomly coded within the N pulses of the dwell. Note that there is an offset applied to the desired random input phase by

microwave components such as the transmitter, which can be well characterized with a transmit loop-back path that routes the transmitter output to the receiver. In practice, $T_1(n)$ and $T_2(n)$ include the system response through a loop-back path and recorded on a pulse-to-pulse basis. Assuming an impulse response from the scatterers, denote the raw received voltages before phase decoding at each channel as $R_1(n)$ and $R_2(n)$ respectively. After digitization, the random starting phase is removed from the received voltages $R_1(n)$ and $R_2(n)$ as

$$V_1(n) = R_1(n)\, T_1^*(n), \tag{22}$$

$$V_2(n) = R_2(n)\, T_2^*(n). \tag{23}$$

Here, n=1,2,.., N where N is the number of pulses within the dwell. The conjugate multiplication with T_1^* and T_2^* are intended to be done on a range profile basis, such that the resultant voltages V_1 and V_2 are equivalent to received echoes using a phase coherent transmitter. At a given range bin m, leakage from the "wrong" channel is superimposed on the desired return. The resultant echoes X_1 and X_2 corresponding to channels 1 and 2 are expressed as

$$X_1(m, n) = V_1(m_1, n)\ +\ R_2(m, n). \tag{24}$$

$$X_2(m + \tau, n) = V_2(m + \tau, n)\ +\ R_1(m + \tau, n). \tag{25}$$

Note that the time lag in transmission has been retained by the use of "fast-times" that are separated by lag τ in equations (24) and (25). For convenience, we approximate the discrete time cross-covariance C_{12} between X_1 and X_2 as the continuous time definition.

$$\sum_{n=1}^{N} X_1(m, n) X_2^*(m + \tau, n) \approx C_{12}(m, \tau) \tag{26}$$

$$C_{12}(m, \tau) = \int_{\infty}^{\infty} X_1(m, T) X_2^*(m + \tau, T) dT \tag{27}$$

Equations (26) and (27) are true when the number of pulses N is sufficiently large. Now X_1 and X_2 can be expanded as

$$C_{12}(m, \tau) = \int_{\infty}^{\infty} [V_1(m, T) + R_2(m, T)] \\ [V_2^*(m + \tau, T) + R_1^*(m + \tau, T)] dT. \tag{28}$$

The cross-covariance can now be rearranged as a superposition of desirable and undesirable terms to

$$\begin{aligned} C_{12}(m, \tau) = \int_{\infty}^{\infty} &[V_1(m, T) \cdot V_2^*(m + \tau, T) \\ &+ V_1(m, T) \cdot R_1^*(m + \tau, T) \\ &+ R_2(m, T) \cdot V_2^*(m + \tau, T) \\ &+ R_2(m, T) \cdot R_1^*(m + \tau, T)] dT. \end{aligned} \tag{29}$$

We identify the first term in (29) as the desired covariance that we wish to measure. The last three terms constitute undesirable leakage that contaminates the cross-covariance measurement. We factor out commonalities between terms by assuming that the underlying random process is wide sense stationary and expressing the first term using the Pearson-Neuman definition of correlation as

$$\int_\infty^\infty V_1 V_2^*(m+\tau, T)dT = c_{12}(\tau) \cdot \sqrt{\int_\infty^\infty V_1^2(m,T)dT}$$
$$\sqrt{\int_\infty^\infty V_2^2(m,T)dT} \tag{30}$$

The terms inside the square root sign in (30) are the expected values of received power at range bin m. Since the time-series at V_1 and V_2 are recorded using the same receiver and phase decoding is subsequently accomplished on the same time-series, it appears reasonable to assume that the power expectations are equal. We therefore replace the geometric mean in (30) with the power expectation at channel 1 as

$$\int_\infty^\infty V_1 V_2^*(m+\tau, T)dT = c_{12}(m,\tau) \cdot \int_\infty^\infty V_1^2(m,T)dT. \tag{31}$$

Assuming wide sense stationarity and invoking discrete-time equivalence, further simplifications can me made as

$$\int_\infty^\infty V_1 V_2^*(m+\tau, T)dT = c_{12}(m,\tau) \cdot \sum_{n=1}^N V_1^2$$
$$\approx N^2 |v_1|^2 c_{12}(m,\tau), \tag{32}$$

where c_{12} ia obtained by setting $\delta k = 0$ in (59) and (62). The undesirable leakage terms in (29) can be simplified by recognizing that they differ from the first term by virtue of having incoherent phases propagated from R_1 and R_2. However, the magnitudes of R_1 and R_2 are the same as V_1 and V_2 respectively. Assuming wide sense stationarity and invoking discrete-time equivalence, the undesirable leakage terms in (29) can be expressed as

$$\int_\infty^\infty V_1(m+\tau, T) \cdot R_1^*(m+\tau, T)$$
$$+ R_1(m+\tau, T) \cdot V_2^*(m+\tau, T)$$
$$+ R_1(m+\tau, T) \cdot R_2^*(m+\tau, T)]dT \tag{33}$$
$$\approx \sum_{n=1}^N |V_1||R_1| + \sum_{n=1}^N |R_2||V_2| + \sum_{n=1}^N |R_2||R_1|$$
$$= 3N|v_1|^2$$

Comments about the statistics of the desired cross-covariance $V_1 \cdot V_2(m,\tau)$ and the undesirable leakage terms are in order. Since the desired cross-covariance is coherent on a pulse-to-pulse basis, it add up in phase during the

accumulation of covariance. The magnitude of the accumulated covariance is therefore proportional to N^2 when the scattering process has low spectrum width. By contrast, the incoherent nature of R_1 on a pulse-by-pulse basis results in the undesirable leakage term $V_1 R_1$ to be accumulated such that it is proportionate to N. This is because the power corresponding to R_1 adds up during covariance accumulation. The net result of all this is that the inter-channel isolation I simplifies to

$$\langle I \rangle = \frac{N c_{12}(m,\tau)}{3} \tag{34}$$

In the presence of thermal noise, inter-channel leakage power adds up with noise power. This is because thermal noise is incoherent by definition. To capture the corresponding degradation of the signal, we define a term Signal to Leakage plus Noise power Ratio ($SLNR$). When the population of scatterers is homogeneously ubiquitous and the RMS velocity turbulence is small, $SLNR$ can be approximated as

$$\langle SLNR \rangle = \frac{1}{\frac{1}{I} + \frac{1}{SNR}} \tag{35}$$

where SNR is the signal to thermal noise power ratio. The standard deviation of the Doppler estimate is given by

$$SD(V_d) = \frac{\lambda^2}{32\pi^2 M |c_{12}(\delta k = 0, \tau)|^2} \cdot$$
$$\left\{ \left[1 + \frac{1}{SLNR} \right]^2 - |c_{12}(\delta k = 0, \tau)|^2 \right\} \tag{36}$$

where, $c_{12}(\delta k = 0, \tau)$ is the correlation between the voltages V_1 and V_2 and obtained by setting $\delta k = 0$ in equations (59) and (61). M is the number of independent samples available in the dwell and λ is the radar wavelength. Corresponding to equation (18), the estimators for Doppler phase and velocity are related to the covariance $X_1 X_2^*$ at lag τ as

$$\langle \psi \rangle = \angle \left[X_1 X_2^*(\tau) \right], \tag{37}$$

$$\langle v_d \rangle = \frac{1}{2k\tau} \langle \psi \rangle, \tag{38}$$

To conceptually validate the the starting phase pulse rejection technique, Monte-Carlo simulations of the time-series V_1 and V_2 were probed. The spectra estimated from the V_1 and V_2 time-series were used as a diagnostic to investigate artifacts tied to the underlying random process. The reasoning is that stationary random processes are completely defined by their spectra, much like random variables are completely defined by probability density functions. In Fig. 8a, leakage from the wrong channel is clearly visible at around -5 m/s in the absence of random phase coding. However, the use of N=1000 pulses rejects leakage from the undesirable channel by virtue of whitening. Over 1000 pulses in the dwell with unique starting phase signatures, we see that the cross-channel isolation simulations follow the theoretical prediction implied by equation (33). Differences between theory and simulations may, in part, be attributed to floating point precision induced

limitations and improper Monte-Carlo sampling of the small numbers being computed. In Figure 8b, the folding behavior of various spectral and time-domain algorithms are
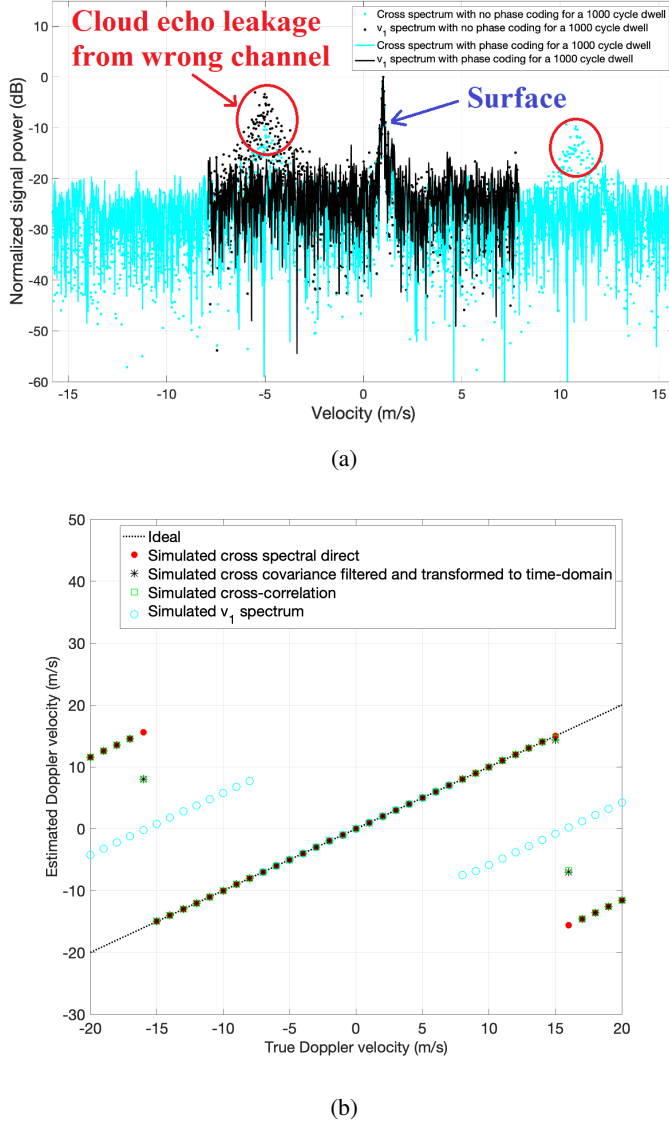
arises for choosing optimal weights of the DFT coefficients for Doppler velocity estimation. One potential answer is to use all the available weights after noise filtering and transform to the time-domain. Another solution is to smooth the

(a)

(b)

Fig. 8: (a) Power spectrum of simulated time-series V_1 and V_2 for 1000 pulses with unique random starting phases within the dwell (i.e. $N = 1000$). Note that the cloud echo leakage from the "wrong" channel is visible with no phase coding but completely whitened when a random starting phase signature is employed. (b) Doppler velocities estimated from cross-correlation of V_1 and V_2 at short lags show reduced folding in Doppler velocity and a wider Nyquist interval. Direct cross-spectral methods are robust to folding.

compared. As expected, the longest lag corresponding to the v_1 auto-spectrum exhibits the narrowest Nyquist interval. Cross-covariance and cross-spectral methods have wider Nyquist intervals by virtue of sampling at a finer lag. The cross-spectra were accessed by setting the lag to be exactly half the pulse repetition time. Once the cross-spectrum is obtained using standard windowing and fast fourier transforms, a dilemma
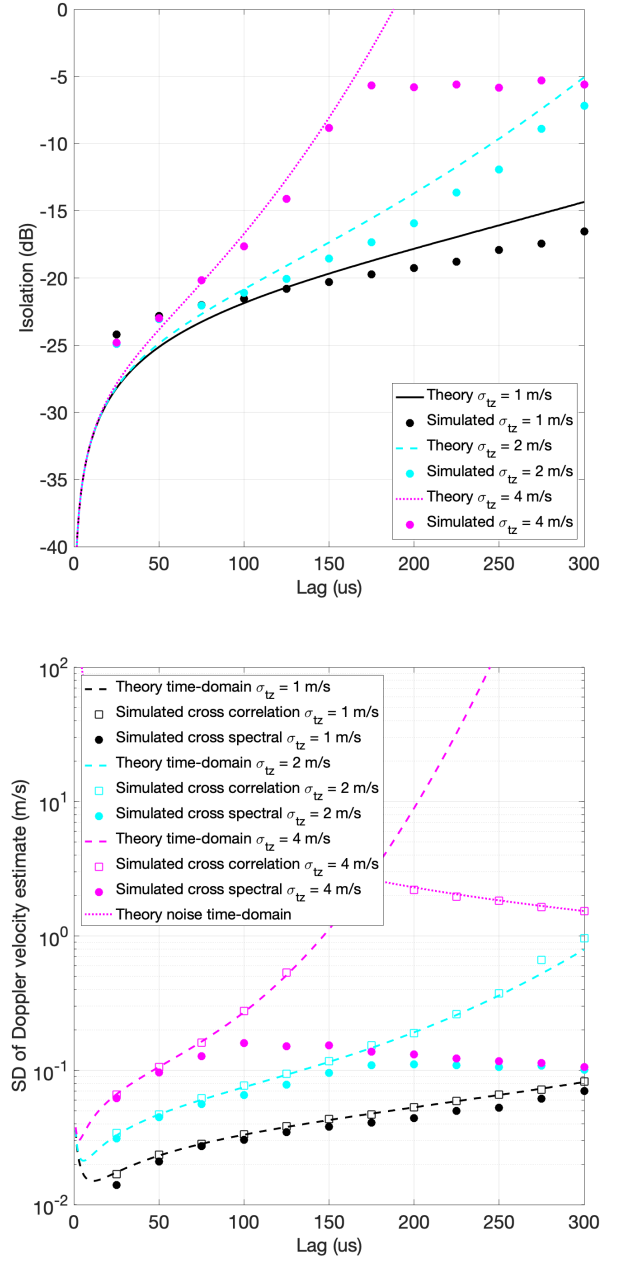

Fig. 9: (a) Isolation and (b) standard deviation of Doppler velocity estimates using the starting phase diversity velocimetry technique as a function of lag (μs). At a relatively high spectrum width of 4 m/s, lags greater than 50 μs show an exponential degradation of isolation. The same 50 us lag results in precision better than 0.1 m/s for spectrum width up to 4 m/s. Parameters - Radar frequency 95 GHz, dwell time 100 ms, $SLNR$ 30 dB and repetition time 100 μs.

DFT coefficients and apply a threshold for spectral moment estimation using the Bartlett method. However, the nearly

identical behavior of the joint time-frequency domain cross-spectral algorithm and the cross-correlation pulse-pair method shows that there is little benefit to the computational penalty incurred. For these reasons that are apparent in Fig. 8b, we only investigate the fully time-domain cross-correlation pulse-pair and the fully cross-spectral algorithms for Doppler velocity estimation in the rest of this work.

Fig. 9 shows isolation and standard deviation of the Doppler estimate as a function of lag for various spectrum of the random process. In Fig. 9a, we see that isolation is a strong function of lag. This is because it is a scaling of the correlation function that defines the wide sense stationary random process as seen in equation (33). As the cross-correlation function evaluated at the lag decreases, inter-channel isolation approaches 0. By the same measure, inter-channel isolation approaches $\frac{N}{3}$ as the cross-correlation function evaluated at the lag increases. In Fig. 9b, we see that the standard deviation of the Doppler estimate using the phase diversity technique varies with the chosen lag. Both theory and simulations show an increase in velocity estimation errors at short lags. This is a direct consequence of the scaling at short lags, wherein small changes in phase are multiplied by a large constant to result in high velocities. For the relatively large spectrum width of 4 m/s, we see that the standard deviation of the time-domain cross-correlation algorithm increases exponentially with lag. However, this exponential increase is bound by the standard deviation of noise at the corresponding lag [45]. Note that the standard deviation noise is solely a function of lag and invariant to the level of RMS velocity turbulence. Notwithstanding, the cross-spectral algorithm vastly outperforms its time-domain equivalent for the large spectrum width of 4 m/s. For lower spectrum width, the outperformance of the cross-spectral algorithm relative to the time-domain cross-correlation algorithm is less dramatic. But even when the data points available for spectral estimation is low corresponding to a spectrum width of 1 m/s in the black curves, the outperformance is still visible in Fig. 9b. For these reasons, it is clear that it is advantageous to set the lag to be exactly one half the pulse repetition time in order to gain access to cross-spectral algorithms for Doppler velocity estimation.

Fig. 10 shows the performance of starting phase velocimetry as a function of Signal to Noise power Ratio (SNR) and Signal to Leakage power Ratio (SLR). In Fig. 10a, both theory and simulations show that there is little improvement in inter-channel isolation beyond 10 dB. For the employed dwell time of 100 ms, the penalty incurred in isolation is relatively small even at an SNR of 0 dB. Notwithstanding, inter-channel isolation degrades as a function of SNR. This is because the accumulated magnitude of cross-covariance starts approaching the improvement N as the signal becomes noise-like. For large SNR, the the accumulated magnitude of cross-covariance approaches N^2. While theory and simulations both predict a degradation in isolation with degrading SNR, some differences remain. This may be attributed, in large part, to the imprecision of the $\frac{1}{1+\frac{1}{SNR}}$ approximation employed in the theoretical analysis to capture the degradation in covariance magnitude as a function of thermal noise. Fig. 10b shows that

inter-channel isolation is invariant to the Signal to Leakage power Ratio. This is because the definition of isolation employed in this work as the spilled power in the cross-channel relative to the source of leakage power in the primary channel. Fig. 10c shows the standard deviation of Doppler velocity estimate as a function of Signal to Leakage and Noise power Ratio (SLNR). Since the degradation in the estimated Doppler standard deviation due to SNR is identical to the degradation due to SLR, there is little need to discrimnate differences in Doppler standard deviation performance between the two. This is unlike Isolation, where Fig. 10a and Fig. 10b show a clear difference in performance due to SNR and SLR. Notwithstanding, Fig. 10c shows that the cross-spectral algorithm has better immunity to thermal noise and leakage at all lags. For low SNR, the relative improvement in precision in the cross-spectral algorithm relative the time-domain cross-correlation algorithm is nearly an order of magnitude. Note that the outperformance of the cross-spectral algorithm as a function of $SLNR$ holds regardless of lass, provided it is short enough to ensure adequate sampling of the cross-correlation function that defines the random process. The only case where the time-domain cross-correlation algorithm performs as well as the cross-spectral algorithm is at high SNR and at short lags such as 25 μs and 50 μs.

Fig. 11 shows the performance of the starting phase pulse rejection technique as a function of spectrum width. In Fig. 11a, we see that inter-channel isolation degrades nearly exponentially as a function of spectrum with for long lags such as 100 μs. Both theory and simulations predict that inter-channel isolation ultimately vanishes as spectrum width increases. However, at large spectrum width and long lags such as 100 μs differences arise in the isolation predicted by theory and simulation. This is because the discrete-time approximation employed in the theoretical analysis is no longer valid for the relatively short dwell time of 100 ms used. While the simulation results are more trustworthy than theory for the long lag of 100 ms and spectrum width larger than 7 m/s, Doppler estimates in this part of the design curve are not useful in practice for systems engineering. Both the shorter lags corresponding to 25 μs and 50 μs yield inter-channel isolation of atleast 20 dB for spectrum width up 6 m/s. However, the cross-spectral implementation of the 50 μs lag corresponds to a relatively larger unambiguous range of 15 km. This makes the 50 μs lag a practical choice for engineering a system. Fig. 11b shows the standard deviation of the Doppler velocity estimate as a function of spectrum width. The longest lag of 100 μs increases exponentially as a function of spectrum width. However, this is bound by the standard deviation of phase due to white noise scaled to the corresponding lag of 100 μs [45]. Note that the standard deviation of noise at the shorter lags of 25 μs and 50 μs are above the Y-axis scale maximum used in Fig. 11b. While the relative outperformance of the cross-spectral algorithm relative to the the time-domain cross-correlation algorithm is dramatic at the long lag of 100 μs, it is still visible at shorter lags at large spectrum widths. Note that cross-spectral algorithms also allow for intuitive filtering of non-uniform beam filling (NUBF) at ranges just above the surface where echoes from
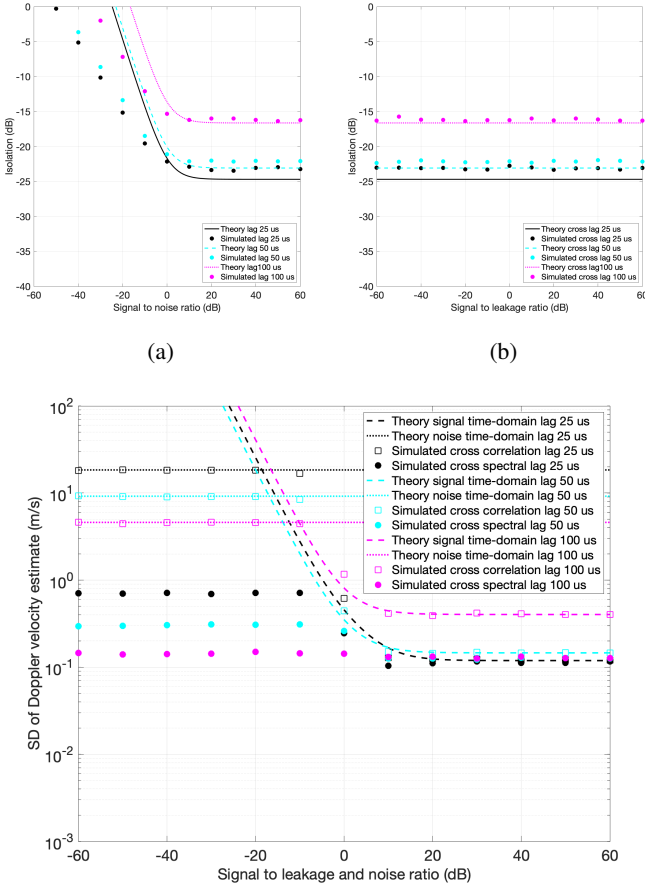
(a)

(b)

Fig. 10: (a) Inter-channel isolation as a function of Signal to Noise power Ratio (SNR). Lags of 50 μs and shorter yield isolation better than 20 dB for SNR 0 dB. (b) Isolation as a function of Signal to Leakage power Ratio shows that the definition used here is immune to this variable. This is because the radar cross section equivalent is common to both channels. (c) Standard deviation of Doppler velocity estimates using the starting phase diversity velocimetry technique as a function of Signal to leakage and noise power Ratio (dB). Lags greater than 30 us result in a precision better than 0.2 m/s for SNR exceeding 20 dB. For lower SNR, the cross spectral algorithm has better immunity than the time-domain pulse-pair algorithm. Parameters - Radar frequency 95 GHz, dwell time 100 ms, spectrum width 4.0 m/s and repetition time 100 μs.
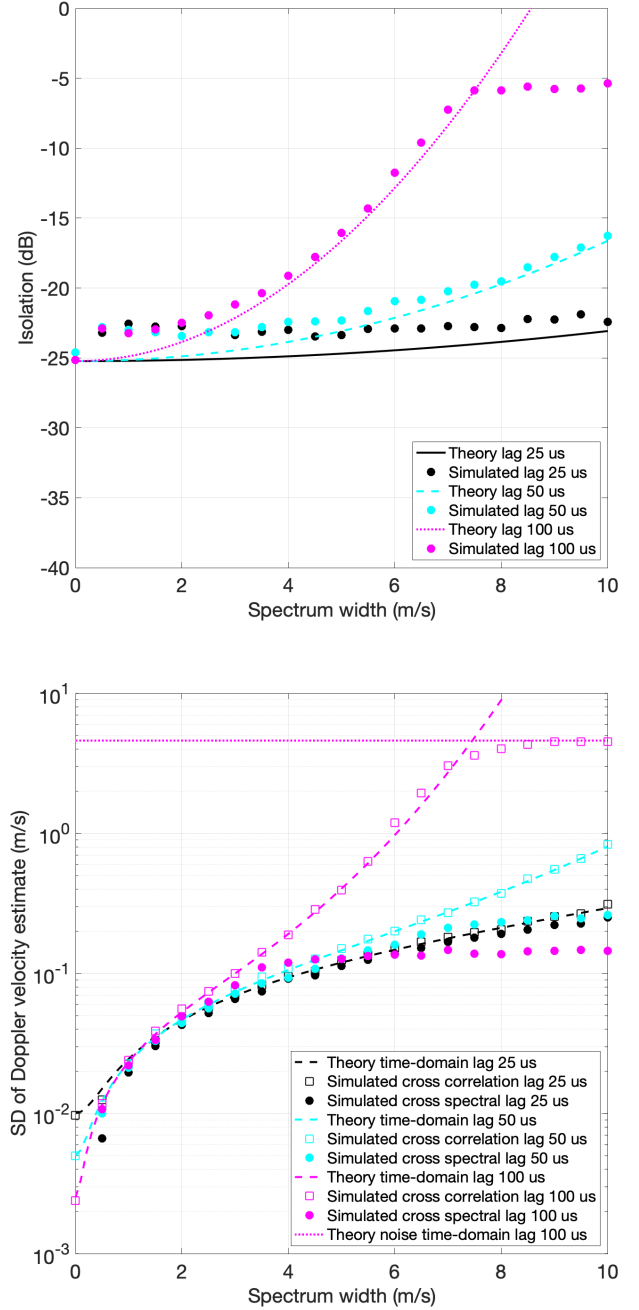

Fig. 11: Standard deviation of Doppler velocity estimates using the starting phase diversity velocimetry technique as a function of Spectrum width (m/s). A 50 μs lag results in precision better than 0.2 m/s for spectrum width up to 2 m/s. Parameters - Radar frequency 95 GHz, dwell time 100 ms, $SLNR$ 30 dB and repetition time 1 ms.
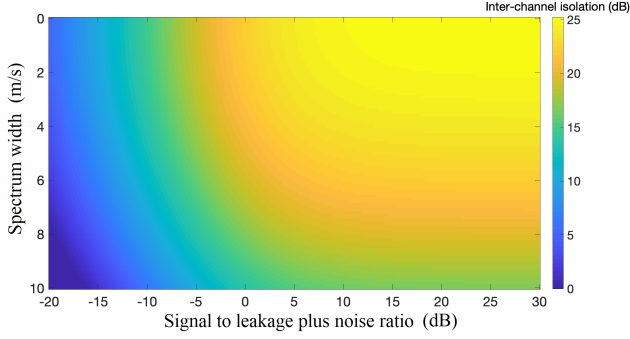
Fig. 12: Theoretical predictions of inter-channel isolation using the phase diversity velocimetry technique. Isolation remains is better than 20 dB for $SLNR$ exceeding 0 dB and spectrum width less than 5 m/s.
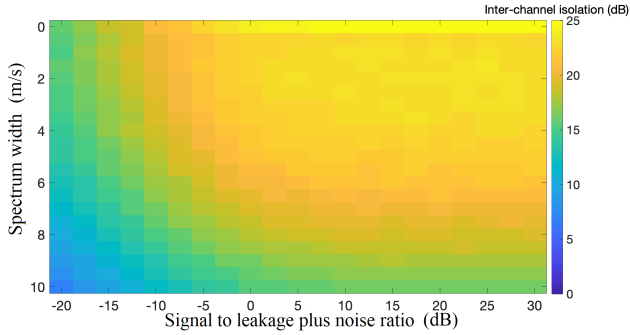

Fig. 13: Simulation predictions of inter-channel isolation using the phase diversity velocimetry technique. Simulation results also show that isolation remains robustly above 20 dB for $SLNR$ exceeding 0 dB and spectrum width less than 5 m/s.
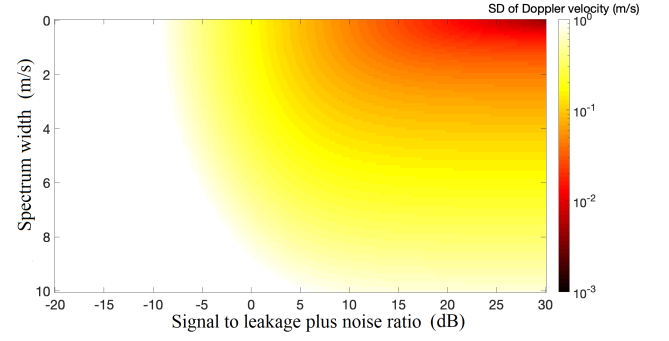

Fig. 14: Theoretical predictions of Doppler velocity estimate standard deviation using the starting phase diversity velocimetry technique. Precision is atleast 0.1 m/s for $SLNR$ greater than 0 dB and spectrum width greater than 4 m/s. Parameters - Radar frequency 95 GHz, dwell time 100 ms, $SLNR$ 30 dB and repetition time 1 ms.
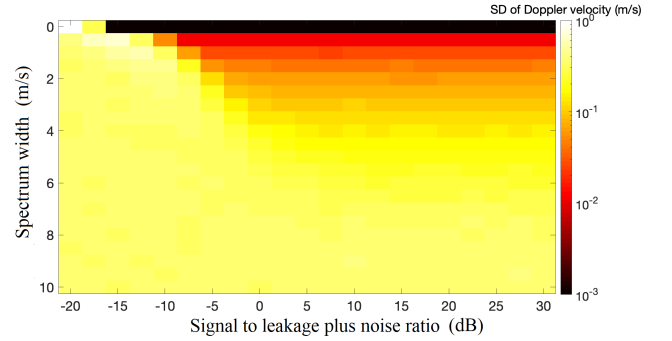

Fig. 15: Simulation predictions of Doppler velocity standard deviation using the time-domain cross-correlation algorithm. The agreement of theory and simulations in regions of $SLNR$ > 10 dB and 0.5 < spectrum width < 4 validates the methodology employed. Parameters - Radar frequency 95 GHz, dwell time 100 ms and repetition time 1 ms.
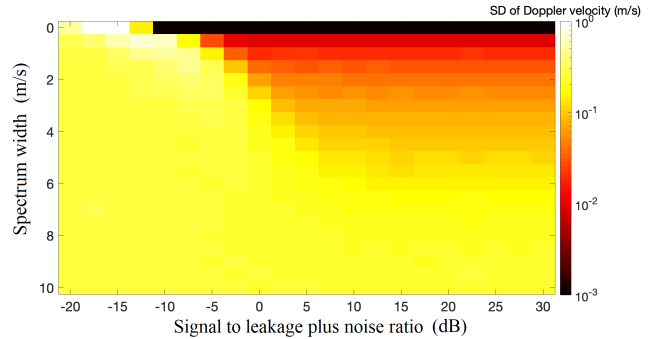

Fig. 16: Simulation predictions of Doppler velocity standard deviation using the cross-spectral algorithm. Note the improved performance of the cross-spectral algorithm relative to the time-domain cross-correlation algorithm in the space spanned by $SLNR$ > 0 dB and 4 m/s < spectrum width < 6 m/s. In addition, cross-spectral algorithm allows filtering of non-uniform beam filling. Parameters - Radar frequency 95 GHz, dwell time 100 ms and repetition time 1 ms.

rain are often superimposed on surface return. Cross-spectral filtering can also be important when multiple hydrometeor species are present within the antenna footprint at the 400 km typical in spaceborne cloud radars. Note that the time-domain cross-correlation algorithm requires unimodal spectra and may not yield physically meaningful Doppler velocity estimates in the presence of non-uniform beam filling. The net result of all this is that a lag of 50 μs with a pulse repetition time of 100 μs thats allows the cross-spectral algorithm to be implemented is a robust choice.

Fig. 12 and Fig. 13 show the inter-channel isolation error space as a function of spectrum width and Signal to Leakage plus Noise power Ratio (SLNR). While isolation performance discrimates thermal noise from leakage, Fig. 10 has already dealt with the differences. Both theory and simulations predict inter-channel isolation of atleast 20 dB for the employed dwell time of 100 ms in the error space spanned by spectrum width less than 6 m/s and $SLNR$ exceeding 0 dB. To partitioning $SLNR$ to an appropriate SNR and SLR to design the system, we recognize that that an SLR of 0 dB corresponds to the physically meaningful case where scatterers are nearly ubiquitously in range. For example, a stratiform precipitation event corresponds to an SLR of 0 dB. In order to successfully probe a stratiform precipitation event, Fig. 12 and Fig. 13 along with equation (35) calls for an SNR requirement of approximately 3 dB for an inter-channel isolation better than 20 dB for spectrum width upto m/s. Therefore, we conclude that pulse rejection can only be physically meaningful when the SNR is relatively high. This result is qualitatively consistent with empirical performance reported in [24]. Note that traditional pulse-pair methods used in conjunction with ground based radar systems have a more graceful degradation of performance as a function of SNR.

Figures 14, 15 and 16 show the standard deviation of the Doppler velocity estimate in the error space spanned by spectrum width and $SLNR$. Theoretical predictions in Fig. 14 agree reasonably well with simulated performance of the time-domain cross-correlation algorithm for $SLNR$ exceeding 0 dB and spectrum width between 0.25 m/s and 6 m/s. For spectrum width less than 0.25 m/s, the assumption that the echo coherence time is comparable to lag employed in theoretical analysis is violated. For spectrum width above 6 m/s, the discrete-time approximation of the random process is imprecise for the short dwell time of 100 ms that is used. Fig. 16 shows the out-performance of the cross-spectral algorithm relative to the time-domain cross-correlation algorithm in the error space spanned by $SLNR > 0$ dB and 4 m/s < spectrum width < 6 m/s [10]. The reason for this relative out-performance is twofold. First, the discrete Fourier transform (DFT) coefficients are approximately identically and independently distributed (i.i.d). For spectral Doppler velocity estimation, DFT coefficients with power levels close to the spectral peak power are most meaningful. As the spectrum width increases, corresponding fluctuations at a random process level are partially offset by the availability of a higher number of data points with high power relative to the cross-spectral peak. Second, the precision of the time-domain pulse-pair cross-correlation algorithm relies on phase estimates from

a single lag that degrades with spectrum width. The net result of all this is that the cross-spectral algorithm is the most robust choice at millemeter wavelengths and there is significant benefit to setting the lag between the channels to be exactly half the pulse repetition time. Furthermore, cross-spectral algorithm allows filtering of non-uniform beam filling due to the presence of both the surface and rain echoes in the shallow troposphere.

V. SUMMARY AND FUTURE WORK

In this work, we investigated a W-band radar that transmits two closely spaced pulses within a repetition time and estimates Doppler velocity by cross-correlating voltages corresponding to the same range-bin. The unambiguous Doppler velocity is now dependent on the time lag between the two transmitted pulses, while unambiguous range is a function of the chosen pulse repetition interval. Echoes corresponding to each transmitted pulse were isolated by synthesizing orthogonal channels. Earlier work on pulse compression based methods for orthogonal channel synthesis on synthetic aperture radars have been shown to be limited to cases where the distribution of scatterers is sparse within a range profile [18]. While point-target simulations of an up/down chirp pulse compression orthogonal waveform pair performed well at W-band, it was shown that pulse-limited geometries had inter-channel isolation of only 5 dB. This work compromised on SNR improvement associated with pulse compression orthogonal waveform synthesis, and focussed on inter-channel isolation by rejecting echoes from the undesired channel. Since the orthogonal channel synthesis techniques investigated herein were based on rejecting inter-pulse spillage without the use of pulse compression, they are referred to as pulse rejection. Two implementations of pulse rejection velocimetry using the frequency and starting phase of sinusoidal bursts were investigated.

The first pulse rejection technique used frequency diversity to synthesize orthogonal channels and transmits successive pulses at each frequency. The transmission sequence of the frequency separated pulses f_1 and f_2 is reversed every pulse repetition time, while retaining the lag separating the pulses. The phase of the f_1/f_2 and f_2/f_1 sequences was estimated by cross-correlating received voltages from the two channels. Doppler velocity was then retrieved using the sum of the phases from the two sequences. It was shown that the standard deviation of Doppler velocity estimates made with frequency domain velocimetry is strongly dependent on the range extent of scattering. This is because fading may be interpreted as the superposition Σe^{-2jkR_n}, where k is the radar wavenumber and R_n is the range to each scatterer. If the variation in R_n is small, the impact of fading is relatively muted. For beam-limited radar observation geometries, the impulse response of surfaces with low RMS heights are often naturally limited in range extent [37]. As the range extent of scattering increases, the impact of fading becomes larger and the precision of the Doppler velocity estimate degrades accordingly. Together, these are consistent with empirical demonstrations of the frequency diversity velocimetry technique [24] contrasting

beam-limited performance of surface observations from cloud observations in a low spectrum width case study.

The second pulse rejection technique uses the starting phase of sinusoidal transmit waveforms to synthesize two orthogonal channels over N pulses of a dwell. But since the phase of the transmitted pulse is known apriori, it is compensated on receive by multiplying the corresponding received range profile with the complex conjugate of the transmit phasor. This is similar to "coherent-on-receive" processing used in magnetron based radar systems. While the synthesis of orthogonal pulses using starting phase have been routinely employed in ground based precipitation radars, this work reports the first investigation of starting phase pulse rejection for Doppler velocity estimation on space-borne cloud radars at millimeter wavelengths. Contrary to frequency diversity velocimetry, this method retains coherence and a high precision for the Doppler velocity estimates without regard to the range extent of of scattering. A limitation of this starting phase velocimetry approach is that it provides limited isolation when a limited number of samples of the stationary random process are acquired. Notwithstanding, the results obtained by theoretical analysis and simulations demonstrated the robustness of phase diversity velocimetry for spectrum width upto 6 m/s (corresponding to normalized spectrum width of 0.22). At millimeter wavelengths, the cross-spectral algorithm that uses a lag exactly half the pulse repetition time was shown to more robust than the time-domain cross-correlation pulse pair algorithm. A significant advantage is that it requires no additional RF hardware relative to what is already available in typical space-borne cloud radar systems [5][6]. Further research on superimposing starting phase diversity velocimetry with upcoming mission concepts such as Displaced Phase-Center Antenna (DPCA) [46][47] and other techniques [17][48] is planned. Investigations of high resolution fully polarimetric synthetic aperture radars using starting phase diversity are also in order.

ACKNOWLEDGMENT

REFERENCES

[1] B. Pollard and G. Sadowy, "Next generation planetary radar for safe planetary landing," in *Aerospace Conference*. Big Sky, MT: IEEE, 2005.

[2] A. Seiff, "Mars atmospheric winds indicated by motion of the viking landers during parachute descent," *J. Geophys. Res.*, vol. 98, pp. 7461–7474, 1993.

[3] C. Chen and B. Pollard, "Radar terminal descent sensor performance during mars science laboratory landing," *Journal of Spacecraft and Rockets*, vol. 51, pp. 1208–1216, 2014.

[4] O. Steffen, "Explore to exploit: A data-centered approach to space mining regulation," pp. 1–11, 2022.

[5] E. Im, C. Wu, and S. Durden, "Cloud profiling radar for the cloudsat mission," *Aerospace and electronic systems magazine*, vol. 20, pp. 15–18, 2005.

[6] S. Tanelli, S. Durden, E. Im, K. Pak, D. G. Reinke, P. Partain, J. Haynes, and R. Marchand, "Cloudsat's cloud profiling radar after two years in orbit : Performance, calibration and processing," *IEEE Trans. Geoscience Remote Sensing*, vol. 46, pp. 3560–3573, 2008.

[7] National academy of sciences, *Thriving on our changing planet : A decadal strategy for earth observation from space*. National academies press, 2017.

[8] W. Tao and X. Li, "The relationship between latent heating, vertical velocity and precipitation processes : the impact of aerosols on precipitation in organized deep convection systems," *J. Geophys. Res.*, vol. 121, pp. 6299–6320, 2016.

[9] S. Tanelli, E. Im, S. Durden, L. Facheris, D. Giuli, and E. Smith, "The effects of non-uniform beam filling on vertical rainfall velocity measurements from a spaceborne radar," *J. Atmos. Oceanic. Tech.*, vol. 19, pp. 1019–1034, 2002.

[10] S. Tanelli, E. Im, L. Facheris, and E. Smith, "DFT-based spectral moment estimators for spaceborne doppler precipitation radar," in *SPIE Remote sensing of the atmosphere, environment and space*, Hangzhou, RC, 2003.

[11] S. Tanelli, E. Im, S. Durden, L. Facheris, D. Giuli, and E. Smith, "Rainfall doppler velocity measurements from spaceborne radar: Overcoming nonuniform beamfilling effects," *J. Atmos. Oceanic. Tech.*, vol. 21, pp. 27–44, 2004.

[12] S. Durden, E. Im, F. Li, W. Ricketts, A. Tanner, and W. Wilson, "Armar : An airborne rain mapping radar," *J. Atmos. Oceanic. Tech.*, vol. 11, pp. 727–737, 1994.

[13] M. Fang and R. J. Doviak, "Spectrum width measured by wsr-88d radar, part i. error sources and statistics of various weather phenomena," *J. Atmos. Oceanic. Tech.*, vol. 21, pp. 888–904, 2004.

[14] S. Haykin, *Communication systems, 4th ed.* John Wiley, 2001.

[15] S. Koboyashi, H. Kumagai, and T. Iguchi, "Accuracy evaluation of doppler velocity on a spaceborne weather radar through a random signal simulation," *J. Atmos. Oceanic. Tech.*, vol. 20, pp. 944–949, 2003.

[16] A. Pazmany, J. C. Galloway, J. Mead, I. Popstefanija, R. McIntosh, and H. Bluestein, "Polarization diversity pulse-pair technique for millimeter wave doppler radar measurements of severe storm measurements," *J. Atmos. Oceanic. Tech.*, vol. 16, pp. 1900–1911, 1999.

[17] A. Battaglia and S. Tanelli, "Polarization diversity for millimeter wave spaceborne doppler radars: An answer for observing deep convection ?" *J. Atmos. Oceanic. Tech.*, vol. 30, pp. 2768–2787, 2013.

[18] G. Krieger, "MIMO-SAR : Opportunities and pitfalls," *IEEE Trans. Geoscience Remote Sensing*, vol. 52.5, pp. 2628–2645, 2014.

[19] D. Giuli, M. Fossi, and L. Facheris, "Radar target scattering matrix measurement through orthogonal signals," *IEEE Proceedings*, vol. 140.4, pp. 233–242, 1993.

[20] C. Chen and P. Vaidyanathan, "Mimo radar ambiguity properties and optimization using frequency hopping waveforms," *IEEE Transactions on Signal Processing*, vol. 56.12, pp. 2870–2877, 2014.

[21] S. Patole, M. Torlak, D. Wang, and M. Ali, "Automotive radars : a review of signal processing techniques," *IEEE Signal Processing Magazine*, vol. 34.2, pp. 22–35, 2017.

[22] Y. Yang and R. Blum, "Mimo radar waveform design based on waveform design based on mutual information and minimum mean square error estimation," *IEEE Trans. Aerosp. Electron. Syst.*, vol. 43.1, pp. 330–343, 2007.

[23] M. Kronauge and H. Rohling, "New chirp sequence radar waveform," *IEEE Trans. Aerosp. Electron. Syst.*, vol. 50.4, pp. 5926–5936, 2008.

[24] V. Venkatesh, L. Li, M. McLinden, M. Coon, G. Heymsfield, S. Tanelli, and H. Hovhannisyan, "A frequency diversity pulse-pair algorithm for extending doppler velocity nyquist range," *IEEE Trans. Aerosp. Electron. Syst.*, vol. 56, pp. 2462–2470, 2020.

[25] X. Li, C. Wang, Z. Qin, J. He, F. Liu, and Q. Sun, "A velocity dealiasing algorithm on frequency diversity pulse-pair for future geostationary spaceborne doppler weather radar," *Atmosphere*, vol. 9.234, 2018.

[26] A. Siggia, "Processing phase coded radar signals with adaptive digital filters," in *Preprints, 21st AMS Conference on Radar Meteorology*. Edmonton, Canada: Amer. Meteor. Soc., 1983, pp. 513–518.

[27] M. Sachidananda and D. Zrnic, "Recovery of spectral moments from overlaid echoes in a doppler weather radar," *IEEE Trans. Geoscience Remote Sensing*, vol. 24, pp. 751–764, 1986.

[28] M. Sachidananda and D. S. Zrnic, "Systematic phase codes for resolving range overlaid signals in a Doppler weather radar," *J. Atmos. Oceanic. Tech.*, vol. 16, no. 10, pp. 1351–1363, 1999.

[29] D. S. Zrnic and D. Schwartzman, "Phase codes for mitigating ambiguities in range and velocity," *J. Atmos. Oceanic. Tech.*, vol. 38, no. 2, pp. 313–329, 2021.

[30] C. Frush and R.J. Doviak and M. Sachidananda and D.S. Zrnic, "Application of the SZ phase code to mitigate range-velocity ambiguities in weather radars," *J. Atmos. Oceanic. Tech.*, vol. 19, pp. 413–430, 2002.

[31] J. Stagliano, J. Alford, J. Hevlin, and D. Nelson, "Phase shifted transmitted signals in a simultaneous dual-polarization weather system," 2009, uS Patent 7,551, 1232.

[32] J. Stagliano, , J. Helvin, J. Alford, and D. Nelson, "Measuring the linear depolarization ratio with the other polarimetric variables," in *Proc, Fourth European Conf. on Radar in Meteorology and Hydrology*, Barcelona, Spain, 1983, pp. 80–83.

[33] D. Zrnic, R. Doviak, V. Melnikov, and I. Ivic, "Signal design to supress coupling in the polarimetric phased array radar," *J. Atmos. Oceanic. Tech.*, vol. 31.5, pp. 1063–1077, 2014.

[34] V. Venkatesh and S. J. Frasier, "Simulation of spaced antenna wind retrieval performance on an x-band active phased-array weather radar," *J. Atmos. Oceanic. Tech.*, vol. 30, pp. 1447–1459, 2013.

[35] R. Engle and W. Granger, "Co-integration and error correction : Representation, estimation and testing," *Econometrica*, vol. 55, pp. 251–276, 1987.

[36] M. Abramovitz and A. Stegun, *Handbook of mathematical functions: with formulas, graphs and mathematical tables*. Dover Publications, 1965.

[37] G. Brown, "The average impulse response of a rough surface and its applications," *IEEE Signal Processing Magazine*, vol. AP-25, pp. 67–74, 1977.

[38] P. Hildebrand and R. Moore, "Meteorological radar observations from mobile platforms," *Radar in meteorology*, pp. 287–314, 1990, D. Atlas (Ed.).

[39] G. Sadowy and coauthors, "The nasa dc-8 airborne cloud radar: Design and preliminary results," in *Int'l. Geosci. & Remote Sensing Symposium*. Singapore, Singapore: IEEE, 1997.

[40] J. Girardin-Gondeau, F. Baudin, and J. Testud, "Comparison of coded waveforms for an airborne meteorological doppler radar," *J. Atmos. Oceanic. Tech.*, vol. 8, pp. 234–246, 1991.

[41] R. J. Doviak and D. S. Zrnić, *Doppler Radar and Weather Observations, 2nd ed.* Academic Press, 1993.

[42] R. J. Doviak, R. J. Lataitis, and C. L. Holloway, "Cross correlations and cross spectra for spaced antenna wind profilers part i: Theoretical analysis," *Radio Sci.*, vol. 31, pp. 157–180, 1996.

[43] A. Pazmany, J. Mead, H. Bluestein, J. Synder, and J. Houser, "A mobile rapid scanning x-band polarimetric (RAXPOL) Doppler radar system," *J. Atmos. Oceanic. Tech.*, vol. 30, pp. 1398–1413, 2012.

[44] S. Durden, R. Beauchamp, S. Graniello, V. Venkatesh, and S. Tanelli, "Dpca-based doppler radar measurements from space: Effects of system errors on velocity estimation performance," *J. Atmos. Oceanic. Tech.*, Submitted in 2022.

[45] S. Kobayashi and T. Iguchi, "Accuracy evaluation of doppler velocity on a spaceborne weather radar through a random signal simulation," *J. Atmos. Oceanic. Tech.*, vol. 20, pp. 944–949, 2003.

[46] S. Durden, P. Siqueira, and S. Tanelli, "On the use of multi-antenna radars for spaceborne precipitation measurement," *IEEE Geoscience and Remote Sensing Letters*, vol. 4, pp. 181–183, 2007.

[47] S. Tanelli, S. Durden, and M. Johnson, "Airborne demonstration of dpca for velocity measurements of distributed targets," *IEEE Geoscience and Remote Sensing Letters*, vol. 13, pp. 1415–1419, 2016.

[48] M. Kumar and V. Chandrasekhar, "Spectral moments from correlated pulse-pairs," *IEEE Trans. Geoscience Remote Sensing*, vol. 58.6, pp. 3841–3853, 2020.

[49] G. Zhang and R. J. Doviak, "Spaced-antenna interferometry to measure crossbeam wind, shear and turbulence: Theory and formulation," *J. Atmos. Oceanic. Tech.*, vol. 24, pp. 791–805, 2007.

APPENDIX

To arrive at a volumetric correlation model and subsequently evaluate Doppler velocity precision for the frequency diversity pulse rejection technique, we evaluate volume scattering integrals that are required to evaluate equation (3) using equations (7), (9) and (11). Following [41], a second order Taylor series expansion of the phase-terms of $V_1(t)$ in equation (6) gives

$$|\vec{R} + \vec{r''}(t)| = r_0 + z''(t) + \frac{x''^2(t) + y''^2(t)}{2r_0}, \qquad (39)$$

where $|\vec{R}| = r_0$. In the rest of this section, we omit the notation "(t)" for scatterer positions. In equation (4), the surface facet co-ordinates x'', y'' and z'' significantly affect the integrand. However, the range to the center of the resolution volume r_0 is invariant of the scatterer locations. Consequently, terms that are dependent on r_0 alone may be factored out of the integral. Substituting (39) in (4), we get

$$I_{x_1} = \int_{x''} exp\{-\frac{x^{2''}}{4r_0^2\sigma_{e\phi}^2}\}exp\{-jk_1 \frac{x''^2}{r_0}\}dx'', \qquad (40)$$

$$I_{y_1} = \int_{y''} exp\{-\frac{y^{2''}}{4r_0^2\sigma_{e\theta}^2}\}exp\{-jk_1 \frac{y''^2}{r_0}\}dy'', \qquad (41)$$

$$I_{z_1} = \int_{z''} exp\{-\frac{z^{2''}}{4\sigma_R^2}\}exp\{-2jk_1z''\}dz''. \qquad (42)$$

In equations (40) and (41), the "x'' and y'' terms correspond to weighting by the azimuth and elevation antenna patterns respectively. Similarly, we expland the phase term in equation (8) using a Taylor series about origin to get

$$I_{x_2} = \int_{x''} exp\{-\frac{(x'' + v_x\tau)^2}{4r_0^2\sigma_{e\phi}^2}\}exp\{-jk_2 \frac{(x'' + v_x\tau)^2}{r_0}\}dx'', \qquad (43)$$

$$I_{y_2} = \int_{y''} exp\{-\frac{(y'' + v_y\tau)^2}{4r_0^2\sigma_{e\theta}^2}\}exp\{-jk_2 \frac{(y'' + v_y\tau)^2}{r_0}\}dy'', \qquad (44)$$

$$I_{z_2} = \int_{z''} exp\{-\frac{(z'' + v_z\tau)^2}{4\sigma_R^2}\}exp\{-2jk_2(z'' + v_z\tau)\}dz''. \qquad (45)$$

where v_x is the mean translational wind-component along x'', v_y is the mean translational wind-component along y'' and v_z is the mean translational wind-component along z''. The cross-covariance of the signals c_{12}^S corresponding to wavenumber k_1 and k_2 in equation (3) can now we written as

$$\begin{aligned} c_{12}^S(\tau) &= \langle V_1 V_2^*(\tau)\rangle \\ &= K \sigma_0 \left(exp\{-2j (k_1 - k_2)r_0\} \right. \\ &\quad \left. J_x J_y J_z \right) \end{aligned} \qquad (46)$$

Here, v_x, v_y and v_z signify the x'', y'' and z'' components of the wind-field respectively. We thereby accommodate all components of relativistic motion between the platform and the resolution volume without having to distinguish between motion of the scatterers and the platform. Following [49], the integrals evaluate to

$$J_x = \int_{x''} \left(exp\{-\frac{(x'' + v_x\tau)^2}{4r_0^2\sigma_{e\phi}^2}\} \right. \\ \left. exp\{-\frac{x''^2}{4r_0^2\sigma_\phi^2}\}exp\{-jk_1 \frac{x''^2}{r_0}\} \right)dx'' \qquad (47)$$

Expressing the wavenumber k_1 as a perturbation around the other radar wavenumber k_2, we get $k_1 = k_2 + \delta k$. This reduces J_x to

$$J_x = \int_{x''} \left(exp\{-\frac{(x'' + v_x\tau)^2 + x''^2}{4r_0^2\sigma_{e\phi}^2}\} \right. $$
$$\left. exp\{j \frac{[k_2(x'' + v_x\tau)^2 - k_2 x''^2 - \delta k\ x''^2]}{r_0}\} \right) dx'' \quad (48)$$

This in turn evaluates to

$$J_x = \sqrt{\frac{\pi r_0^2\sigma_{e\phi}^2}{1 + j2\delta k r_0\sigma_{e\phi}^2}} \exp\{-\frac{2v_x^2\tau^2 k_2^2\sigma_{e\phi}^2}{1 + 4\delta k^2 r_0^2\sigma_{e\phi}^4}\}$$
$$exp\{j\frac{4\delta k r_0 v_x^2\tau^2 k_2^2\sigma_{e\phi}^4}{1 + 4\delta k^2 r_0^2\sigma_{e\phi}^4} + j\frac{4v_x^2\tau^2 k_2 r_0\sigma_{e\phi}^2}{2r_0^2\sigma_{e\phi}^2}\} \quad (49)$$

In a similar manner,

$$J_y \simeq \sqrt{\frac{2\pi r_0^2\sigma_{e\theta}^2}{1 + 4j\delta k r_0\sigma_{e\theta}}}$$
$$exp\{\frac{-v_y^2\tau^2 k_2^2\sigma_{e\theta}^2}{(1 + \delta k^2 r_0^2\sigma_{e\theta}^2)}\} exp\{-4jk_2\delta k v_y\tau^2\} \quad (50)$$

The surface scattering integrals about the co-ordinate z'' can similarly be evaluated as

$$J_z = \int_{z''} \left(exp\{-\frac{(z'' + v_z\tau)^2}{4\sigma_R^2}\} exp\{2jk_2(z'' + v_z\tau)\} \right. $$
$$\left. exp\{-\frac{z''^2}{4\sigma_R^2}\} exp\{-2jk_1 z''\} \right) dz'' \quad (51)$$

$$J_z = \int_{z''} \left(exp\{-\frac{(z'' + v_z\tau)^2 + z''^2}{4\sigma_R^2}\} \right. $$
$$\left. exp\{2jk_2(z'' + v_z\tau) - 2jk_2 z'' - 2j\delta k\ z''\} \right) dz'' \quad (52)$$

$$J_z \simeq \sqrt{2\pi}\sigma_R\ exp\{-2\delta k^2\sigma_R^2\}\ exp\{2jk_2 v_{z''}\tau\} \quad (53)$$

To proceed, we approximate the expectations of $I_{x_1} I_{x_2}$ and $I_{y_1} I_{y_2}$ by themselves. This is tantamount to neglecting fluctuations of v_x and v_y. The reasoning is that the z''-component of velocity causes the most radar signal phase fluctuations and overwhelms sensitivity to x''- and y''-components of fluctuations. Therefore, it suffices to evaluate the ensemble average of the z''-component of velocity alone. To evaluate the expectation of J_z, we decompose v_z into its mean and fluctuating components.

$$\langle J_z \rangle = \sqrt{2\pi}\sigma_R\ exp[-2\sigma_R^2\delta k^2\ ]$$
$$\int_{-\infty}^{\infty} (\exp\{2jk_2\ [(v_{mz} + v_{tz})\tau]\}) p(v_{tz}) dv_{tz} \quad (54)$$

$$\langle J_z \rangle = \sqrt{2\pi}\sigma_R\ exp[-2\sigma_R^2\delta k^2\ ] exp\{2jk_2\ v_{mz}\tau\}$$
$$\int_{-\infty}^{\infty} (\exp\{2j\ k_2\ v_{tz}\tau\} p(v_{tz})) dv_{tz} \quad (55)$$

where, $p(v_{tz})$ is the probability density function of the z''-component of velocity. The specific form of (55) depends on the probability density function (PDF) that is characteristic of the scatterers. While the facets of a solid surface are static, the only apparent motion is due the relative motion of the spacecraft. The PDF expressing motion of solid surface facets may therefore be viewed to be a sub-set of independently moving facets. For the overarching case of dynamically moving facets, the PDF is a function of the spatial scale of the resolution volume and the sensitivity of the viewing geometry to the spread in vertical velocity. In this case, we approximate the PDF of velocity turbulence as Gaussian [42]

$$\langle J_z \rangle = \sqrt{2\pi}\sigma_R\ exp[-2\sigma_R^2\delta k^2\ ] exp\{2jk_2\ v_{mz}\tau\}$$
$$\int_{-\infty}^{\infty} \left(\exp\{2jk_2 v_{tz}\tau\} \frac{exp\{-\frac{v_{tz}^2}{2\sigma_{tz}^2}\}}{\sqrt{2\pi\sigma_{tz}^2}} \right) dv_{tz} \quad (56)$$

$$J_z \simeq \sqrt{2\pi}\sigma_R\ exp[-2\sigma_R^2\delta k^2]$$
$$exp[-2k_2^2\sigma_{tz}^2\tau^2]\ exp\{2jk_2 v_{mz}\ \tau\} \quad (57)$$

Substituting equations (49), (50) and (57) in (46), the phase and magnitude of the covariance can be expressed as

$$\angle\langle c_{12}(\tau) \rangle = -2\ \delta k r_0 - k_2\ \delta k\ v_x^2\ \tau^2 - k_2\ \delta k\ v_y^2\ \tau^2 - 2k_2 v_{mz}\ \tau, \quad (58)$$

and

$$|\langle c_{12}(\tau) \rangle| = P\ exp\left[-\frac{2v_x^2\tau^2 k_2^2\sigma_{e\phi}^2}{2\delta k^2 r_0^2\sigma_{e\phi}^2 + 1} \right] exp\left[-\frac{2v_y^2\tau^2 k_2^2\sigma_{e\theta}^2}{2\delta k^2 r_0^2\sigma_{e\theta}^2 + 1} \right]$$
$$\cdot\ exp[-2k_2^2\sigma_{tz}^2\tau^2] \cdot exp[-2\sigma_R^2\delta k^2] \quad (59)$$

where the cross-covariance normalization term P is given by

$$P = \left[\frac{2\pi r_0^2\sigma_{e\phi}^2}{1 + 2j\delta k r_0\sigma_{e\phi}} \right]^{1/2} \left[\frac{2\pi r_0^2\sigma_{e\theta}^2}{1 + 2j\delta k r_0\sigma_{e\theta}} \right]^{1/2} \sqrt{2}\sigma_R. \quad (60)$$

The correlation function C_{12}^S for the signal only case may be accessed as

$$C_{12}^S = \frac{c_{12}}{P}. \quad (61)$$

In the presence of thermal noise, the correlation function is given by

$$C_{12} = \frac{1}{1 + \frac{1}{SNR}} C_{12}^S \quad (62)$$

where SNR denotes the signal to noise ratio of power. We note that the expression for the correlation function magnitude in equations (59)-(61) is consistent with the commonly employed model in the community [42] for the case of no frequency diversity (i.e. $\delta k = 0$). Lastly, the formulation for the correlation function herein is generally applicable to beam-filled scenarios such as scattering from surfaces or cloud

particles. Based on the expressions developed in this appendix, the performance of pulse-pair velocimetry algorithms are evaluated in sections III and IV.